

This is the accepted manuscript made available via CHORUS. The article has been published as:

# Superlattice formation in colloidal nanocrystal suspensions: Hard-sphere freezing and depletion effects

Samuel L. Brown, Vijay D. Shah, Maria V. Morrell, Mitchell Zubich, Alexander Wagner, Alan  
R. Denton, and Erik K. Hobbie

Phys. Rev. E **98**, 062616 — Published 26 December 2018

DOI: [10.1103/PhysRevE.98.062616](https://doi.org/10.1103/PhysRevE.98.062616)

# Superlattice Formation in Colloidal Nanocrystal Suspensions: Hard-Sphere Freezing and Depletion Effects

Samuel L. Brown,<sup>1</sup> Vijay D. Shah,<sup>2</sup> Maria V. Morrell,<sup>1</sup> Mitchell  
Zubich,<sup>2</sup> Alexander Wagner,<sup>2</sup> Alan R. Denton,<sup>2</sup> and Erik K. Hobbie<sup>1,2,3</sup>

<sup>1</sup>*Materials & Nanotechnology Program,*

*North Dakota State University, Fargo, North Dakota 58108*

<sup>2</sup>*Department of Physics, North Dakota State University, Fargo, North Dakota 58108*

<sup>3</sup>*Department of Coatings & Polymeric Materials,*

*North Dakota State University, Fargo, North Dakota 58108*

## Abstract

Superlattice formation in dried suspensions of colloidal silver nanocrystals (AgNCs) is investigated through a combination of experiment, theory, and simulation. Using microscopic and spectroscopic techniques, we explore the phase behavior of dried AgNC suspensions, and we model the system using Monte Carlo simulations of a coarse-grained model with an effective pair potential that accounts for the composition of the nanocrystal core, the stabilizing ligand shell, and entropic effects associated with unbound ligand in solution. In the absence of free ligand, the effective potential at ligand contact is purely repulsive and we find superlattice formation at an effective AgNC volume fraction close to that anticipated for hard-sphere freezing. In the presence of free ligand, the effective potential becomes attractive and crystallization is accompanied by phase separation and multiphase coexistence, as anticipated for colloid/polymer mixtures.

## I. INTRODUCTION

In the last two decades, colloidal nanocrystals (NCs) have emerged as a nanotechnology success story. They are the focus of a tremendous amount of research directed at a range of applications (color displays, solar cells and fluorescent labels) and are now found in commercial applications such as ‘quantum dot’ televisions. Since the pioneering work of Murray, Kagan and Bawendi [1], NC ‘superlattices’ – self-assembled ordered arrays – have become a paradigm for NCs as thin solid films. In general, NC superlattices represent a diverse array of core materials, shapes, sizes and properties [2, 3], with transmission electron microscopy (TEM) being the most utilized tool [4, 5]. Although colloidal NCs are often idealized as residing in perfect arrays, in reality nanocrystal superlattices can be challenging to achieve, particularly for small ( $< 10$  nm diameter) NCs. To induce phase ordering, a number of approaches have been utilized [6], with the simplest being the evaporation of a sessile drop on a smooth surface.

Physically, we can understand superlattice formation through a balance of energy and entropy [7, 8], but unique issues can emerge at the nanoscale that present significant challenges to the formalisms commonly used to model microscale colloids. Most notably, these relate to the nature of the nanoparticle interaction potential [9]. Specifically, the additivity assumption – the premise that the total potential can be written as the sum of multiple independent repulsive and attractive parts – becomes invalid for certain heterogenous nanoscale colloids [10–12]. In addition, the role of ligand-ligand interactions [13] and the impact of unbound ligand [14] or polymer [15] on nanocrystal self-assembly [16] remains relatively unexplored computationally.

For metallic or heavily-doped semiconductor NCs, the strong surface coupling between charge carriers and light leads to a unique optical absorption feature that we refer to as the single-particle plasmon [17]. Intuitively, when individual plasmonic NCs assemble into aggregates or ordered superlattices, a collective plasmon emerges that reflects concerted charge oscillations over larger length scales [17–19]. Such effects can be striking for plasmonic NC superlattices and are of considerable current interest for applications in biological sensing [21, 22] and optical engineering [23].

Here, we investigate superlattice formation in dried suspensions of colloidal silver nanocrystals (AgNCs), focusing primarily on the role of both bound and unbound ligand. Our experimental approach utilizes electron microscopy, optical microscopy, and

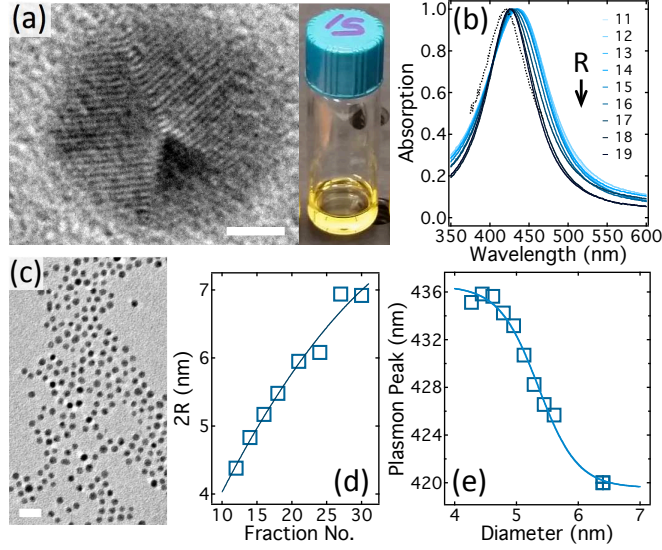


FIG. 1. (color online) (a) TEM image of an individual AgNC with surface facets and planes of atomic crystallinity (2 nm scale). The image on the right is a fraction in toluene. (b) Plasmon absorption peak measured for monodisperse AgNC suspensions of varied nanocrystal size, where the solid curves are for NCs synthesized using Method I (size separated through DGU where the legend denotes fraction number) and the dashed curve is for NCs synthesized using Method II. (c) TEM image of a AgNC fraction cast from a dilute suspension (20 nm scale). (d) Nanocrystal diameter based on TEM plotted *vs.* fraction number with a polynomial fit. (e) Plasmon absorption peak wavelength as a function of nanocrystal diameter with a sigmoidal fit, where the open markers are from Method I and the hatched marker is from Method II. All samples depicted are either dispersed in toluene or cast from toluene.

optical absorption spectroscopy. Computationally, we utilize Monte Carlo simulations with an effective interaction potential that accounts for ligand-solvent interactions, depletion effects, and the effective Hamaker constant of the nanocrystal/ligand pair. In the absence of free ligand, both experiment and simulation suggest superlattice at a critical AgNC volume fraction of 0.17. Because the effective potential is purely repulsive in this limit, we rationalize this through the volume associated with the bound ligand shell, implying that ordering occurs at an effective volume fraction close to that anticipated for hard-sphere freezing. The simulations also clearly demonstrate unbound ligand as an effective depletant in ternary AgNC/ligand/solvent mixtures, with the experiments showing multiphase coexistence analogous to colloid/polymer mixtures.

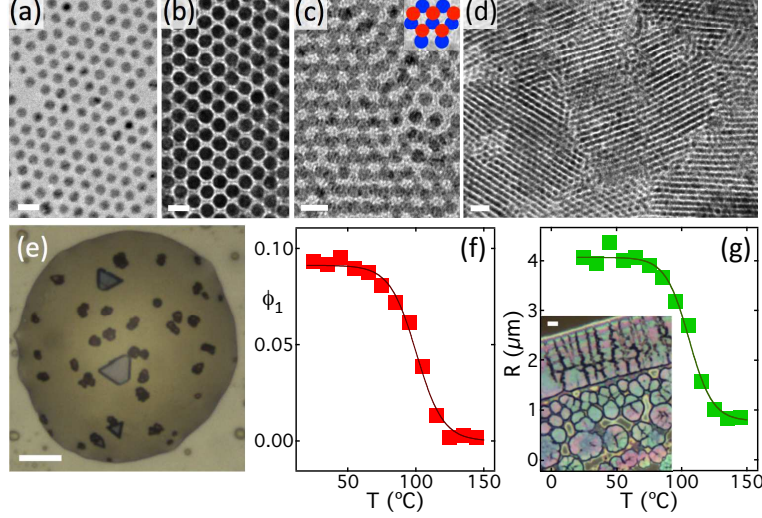


FIG. 2. (color online) (a) TEM image of a AgNC superlattice (Method II) and (b) TEM image of ordered close packing for AgNCs of slightly larger diameter (10 nm scale both images). (c) TEM image of 2-layer packing as depicted in the upper right inset (10 nm scale). (d) Domain boundaries for the suspension depicted in panel (b) (20 nm scale). (e) Reflection optical micrograph of large superlattice domains suspended in a background ‘solvent’ of free ligand (10  $\mu\text{m}$  scale, room temperature). (f) Volume fraction of superlattice from (e) as a function of temperature and (g) the corresponding mean domain size. The inset shows a reflection optical micrograph of the ‘coffee-ring’ deposit for the same suspension after removal of excess ligand (2  $\mu\text{m}$  scale). All samples were cast from toluene.

## II. MATERIALS & METHODS

*Materials:* All solvents and chemicals were purchased from Sigma Aldrich and used without further purification: silver nitrate (> 99 %), silver acetate (99.0 %), sodium borohydride (> 99 %), oleylamine (70 %), 1,2-dodecanediol (90 %), toluene (99.9 %), 1,2-dichlorobenzene (99 %), chloroform (99.98 %), m-xylene (99 %), hexane (95 %), methanol (99.8 %), ethanol (99 %), and 1-propanol (99.5 %).

*Characterization:* TEM images were taken with a JEOL JEM-2100 analytical TEM operated at 200 kV and collected using a GATAN Orius SC1000 bottom-mount CCD. Samples for TEM were drop cast from toluene onto ultrathin lacey carbon TEM grids (400 mesh Cu) and dried slowly under a vial cap. Nanocrystal size distributions were analyzed using

*ImageJ*. For a select subset of the images, the coordinates of the nanocrystal centers were located using *ImageJ* and the various metrics of crystalline order were then computed in *MATLAB* using previous established code [24] that we modified accordingly. The local AgNC area fraction computed in *ImageJ*,  $\phi_A$ , was converted to volume fraction as  $2\phi_A/3$ , which is exact for a coplanar collection of spheres. Optical micrographs were collected over a range of magnifications in both reflection and transmission mode and the area fractions of the observed phases were computed in *ImageJ*. These quantities were then converted to volume fraction using the same factor of  $2/3$ , which in this case represents an approximation. Absorption spectra in the solution state were collected on a Cary 5000 UV-Vis-NIR spectrometer, while absorption spectra for thin solid films were collected *in situ* using a customized upright optical microscope (Olympus BX51) equipped with a CCD camera and  $4\times$ ,  $10\times$ ,  $20\times$  and  $100\times$  objectives. A fiber-coupled Ocean Optics QE65000 spectrometer with a broad-band excitation source (X-Cite 120Q lamp) was used for spectral analysis. Details related to substrate patterning can be found in the Supplemental Material [25].

### III. RESULTS & DISCUSSION

#### A. Nanocrystal synthesis & purification

The AgNCs of interest have diameters of 5-6 nm and were synthesized using two different approaches. In both, the stabilizing ligand is oleylamine. The first (Method I) uses only a solvent, silver acetate precursor, and oleylamine as ligand and reductant [26]. This method produced somewhat polydisperse AgNCs and we used density-gradient ultracentrifugation (DGU) in organic solvents to separate the nanocrystals into size-resolved fractions [27, 28]. The TEM size distribution of the resulting fractions and details related to DGU can be found in the Supplemental Material [25]. Figure 1a shows a TEM image of an individual AgNC and a picture of a typical fraction. Changes in NC size with fraction number are evident in the wavelength of the single-particle plasmon peak (Fig. 1b), where Fig. 1c shows a TEM image of a typical fraction. The mean size of each fraction from TEM is shown in Fig. 1d and the measured size dependence of the plasmon (Fig. 1e) is in agreement with anticipated trends [29, 30]. DGU reduces the amount of excess ligand in the suspensions, but fractions stored in a nitrogen-filled glovebox remained colloidally stable for over a year.

The second scheme (Method II) differs from the first in that the initial mixture (solvent, silver nitrate, and oleylamine) is injected into a hot dodecanediol/dichlorobenzene solution

(180 °C) and allowed to react for 3 min before being cooled to ambient [29, 31]. The additional ‘hot injection’ step in the presence of a modest reducing agent (dodecanediol) improve the sharpness of the AgNC size distribution such that additional size purification is not necessary. Impurities and unbound ligand were then removed *via* varied degrees of washing with polar anti-solvents [25]. As shown in Fig. 1e, the wavelength of the single-particle plasmon for Method II (420 nm) is in agreement with trends exhibited by the size-separated AgNCs synthesized using Method I. Representative TEM images for AgNCs synthesized using Method II are shown in Fig. 2, where typical TEM size distributions can be found in the Supplemental Material [25].

In general, we found that nanocrystal concentration and size uniformity are both critical to superlattice formation, and while the fractions obtained through Method I are monodisperse, the concentration of such fraction was typically insufficient to observe ordering. Hence, all results discussed hereafter in the context of superlattice are for NCs synthesized through Method II, but we retain the discussion of Method I because these results provide a measure of reproducibility, size and quality for AgNCs synthesized with Method II (Fig. 1e).

### B. Self-assembly & characterization

The arrangement of successive layers in TEM is consistent with either *hcp* or *fcc* packing (Fig. 2c) and superlattice was prevalent (Fig. 2d & e). However, we note that large faceted domains (Fig. 2e) were only observed when the samples were cast from a common good solvent in the presence of abundant excess ligand. As shown in (Fig. 2f & g), these domains readily melt at elevated temperatures – consistent with weak attraction – but do not reform on cooling, suggesting that solvent is critical to formation. Suspensions that underwent repeated washing to remove excess ligand (inset to Fig. 2g) did not form these faceted structures [25], which represent the two-phase coexistence of superlattice domains and a disordered ligand-rich phase (background fluid, Fig. 2e). Taken as a whole, these observations suggest that depletion interactions mediated by unbound ligand can play a significant role in AgNC self-assembly, and although several groups have considered depletion in the context of nanocrystal self-assembly [32–36], new approaches to modeling are warranted [37, 38].

Dried samples exhibited an abundance of 3D domain structures that are difficult to quantify in TEM. However, TEM images that exhibited quasi-2D (coplanar) particle ar-

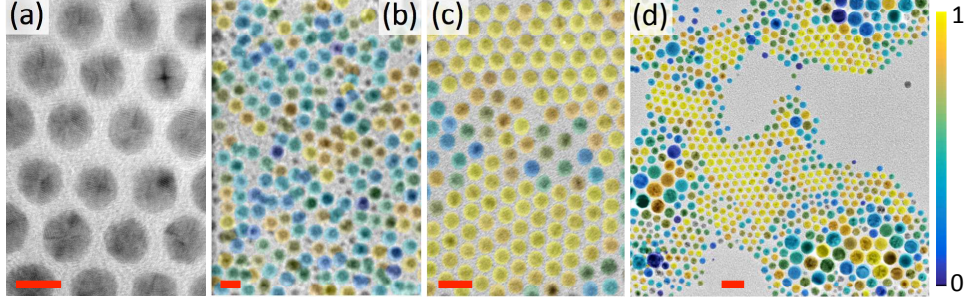


FIG. 3. (color online) (a) TEM image showing AgNC crystal orientation across a superlattice (6 nm scale). (b) Superposition of a TEM image and a shade/color plot (scale at far right) of the local bond-orientational order parameter  $m_6(\mathbf{r})$  defined in the text (10 nm scale) for a disordered sample. (c) A similar superposed TEM image for an ordered sample (10 nm scale) and (d) for local ordering in a polydisperse AgNC sample (20 nm scale).

rangements were digitally processed to obtain the particle centers  $(x,y)$ . From the centers, a number of indicators for long-range crystalline order can be computed to delineate order from disorder. The primary quantities of interest here are the radial distribution function,  $g(r)$ , and the static structure factor [39],  $S(q)$ , where  $q$  is wave vector. We also computed the bond-orientational order parameter,

$$\psi_6(\mathbf{r}_k) = \frac{1}{n_k} \sum_{j=1}^{n_k} \exp(6i\theta_{jk}), \quad (1)$$

where the index  $j$  runs over the  $n_k$  nearest neighbors of particle  $k$  (located at  $\mathbf{r}_k$ ) and  $\theta_{jk}$  is the angle of the bond between particle  $k$  and particle  $j$  as measured with respect to an arbitrary but fixed direction. From  $\psi_6$ , we can compute the useful quantities  $m_6(\mathbf{r}_k) = |\psi_6(\mathbf{r}_k)|$  and  $n_6(\mathbf{r}_k) = |\psi_6^*(\mathbf{r}_k)\langle\psi_6(\mathbf{r}_j)\rangle_j|$ , where  $\langle...\rangle_j$  in the latter expression denotes an average over the nearest-neighbor index  $j$ . As demonstrated by Larsen and Grier [40],  $n_6$  is useful for delineating regions of order and disorder in polydomain samples, and a discussion of the various metrics of long-range order in this context can be found in the recent work of Dillmann *et al* [41]. Examples are shown in Fig. 3, where color/shade-coded plots of  $m_6$  are overlaid on gray-scale TEM images to indicate the local order around each particle. Figure 3d shows the same approach applied to polydisperse AgNCs that nonetheless exhibited local ordered packing, although such TEM images were not used in our analysis.

The macroscopic phase behavior was evaluated from optical micrographs such as those



represented in Fig. 2c-f. Crystalline domains are easily identified as faceted structures in a continuous ligand-rich background, and we use optical images to estimate the volume fraction of the two phases;  $\phi_1$  (superlattice) and  $\phi_2$  (disordered) with  $\phi_1 + \phi_2 = 1$ . Defining the global AgNC volume fraction as  $\Phi_{\text{NC}}$ , and assuming equilibrium phase profiles, the lever rule gives  $\Phi_{\text{NC}} = \phi_1\phi_{\text{NC}} + \phi_2\phi_{\text{F}}$ , where  $\phi_{\text{F}}$  is the AgNC volume fraction in the ligand-rich phase.

### C. Theory & simulation

To model the equilibrium phase behavior, the AgNCs are represented as spherical Ag cores of radius  $a$  coated with a layer of oleylamine ligand of contour length  $d$ . Similarly, free ligands in solution are modeled as effective spheres of radius  $d/2$ . The ligands and solvent molecules (toluene) are modeled implicitly, their properties determining parameters in the effective interparticle pair potential [44–46]

$$v_{\text{eff}}(r) = v_{\text{vdW}}(r) + v_{\text{mix}}(r) + v_{\text{el}}(r) + v_{\text{dep}}(r), \quad (2)$$

where  $v_{\text{vdW}}(r)$  represents van der Waals interactions [46, 47],  $v_{\text{mix}}(r)$  represents the free energy of mixing for ligand and solvent [44, 48, 49],  $v_{\text{el}}(r)$  is the short-range repulsive potential arising from the loss of configurational entropy as the ligand layers undergo elastic compression [44, 45, 50], and  $v_{\text{dep}}(r)$  models depletion interactions induced by unbound ligand [46].

Expressing all lengths in units of the AgNC core diameter ( $2a$ ), the van der Waals potential is [44, 45]

$$v_{\text{vdW}}(r) = -\frac{H}{12} \left[ \frac{1}{r^2 - 1} + \frac{1}{r^2} + 2 \ln \left( 1 - \frac{1}{r^2} \right) \right], \quad (3)$$

where  $H$  is the effective Hamaker constant, which we approximate as the Hamaker constant for bulk Ag interacting across oleylamine. We did not consider toluene explicitly, because for drying suspensions, the ligand layers were assumed to mediate the interactions more than the solvent [44]. Although at low ligand surface coverage the AgNCs may interact across a medium that is primarily toluene, we confirmed that the effective pair potential is insensitive to the resulting change in  $H$ .

The free energy of mixing,  $v_{\text{mix}}(r)$ , is nonzero only when neighboring ligand layers overlap, being a piecewise function of the center-center distance  $r$  between two NCs. In the first regime ( $1 + d < r < 1 + 2d$ ), the ligand layers partially overlap but do not necessarily

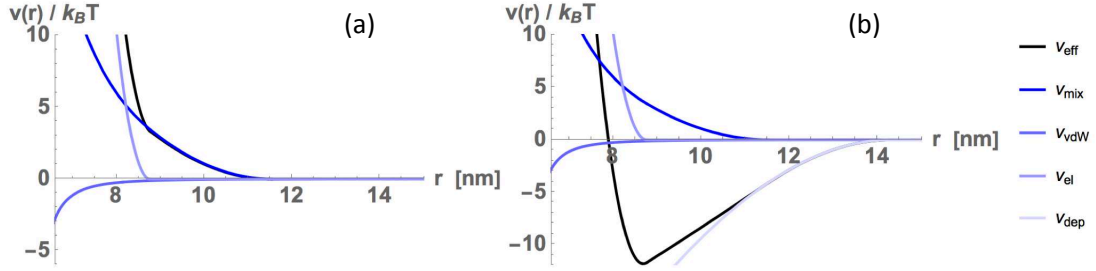


FIG. 4. (color online) Effective pair potential for AgNCs in toluene (a) without depletion interactions and (b) with depletion interactions at average free ligand volume fraction  $\phi_{\text{FL}} = \frac{4}{3}\pi\rho_{\text{FL}}L^3 = 0.558$ . In order of decreasing magnitude at  $r = 8.5$  nm, the curves are (a)  $v_{\text{eff}}$ ,  $v_{\text{mix}}$ ,  $v_{\text{el}}$  and  $v_{\text{vdW}}$ ; (b)  $v_{\text{mix}}$ ,  $v_{\text{el}}$ ,  $v_{\text{vdW}}$ ,  $v_{\text{eff}}$  and  $v_{\text{dep}}$ .

compress [44, 49]:

$$\beta v_{\text{mix}}(r) = \frac{\pi}{2V_s} \phi_{\text{av}}^2 \left( \frac{1}{2} - \chi \right) (r - 1 - 2d)^2, \quad (4)$$

where  $\beta \equiv 1/(k_B T)$ . In the second regime ( $r < 1 + d$ ), the layers strongly overlap and are forced to compress [44, 50]:

$$\beta v_{\text{mix}}(r) = \frac{\pi}{V_s} \phi_{\text{av}}^2 \left( \frac{1}{2} - \chi \right) d^2 \left( 2 \ln \frac{d}{r-1} + \frac{r-1}{d} - \frac{1}{2} \right), \quad (5)$$

where  $V_s$  is the molecular volume of a solvent (toluene) molecule,  $\phi_{\text{av}}$  is the average volume fraction of ligands in the ligand layer ( $1 < r < 1 + d$ ), and  $\chi$  is the Flory parameter [44],

$$\chi = \frac{V_s(\delta_s - \delta_l)^2}{k_B T} + 0.34. \quad (6)$$

Here  $\delta_s$  and  $\delta_l$  are the Hildebrand solubility parameters for the solvent and ligand, respectively, and  $T$  is temperature. In a ‘good’ solvent ( $\chi < 0.5$ ), ligand-solvent interactions contribute to NC repulsion, while in a ‘poor’ solvent ( $\chi > 0.5$ ), ligand-solvent interactions contribute to NC attraction.

The elastic potential models the compression associated with the loss of configurational entropy in the ligand layers when  $r < 1 + d$  [44, 45, 50]:

$$\beta v_{\text{el}}(r) = \pi n \left[ (r - 1) \left( \ln \frac{r-1}{d} - 1 \right) + d \right], \quad (7)$$

where the ligand surface coverage  $n$  is the number of ligands per unit area per NC. Confinement to the NC surface reduces the number of microstates accessible to the ligands,

resulting in a short-range repulsive interaction [44, 50].

The exclusion of depletants from the region between two NCs induces an effective attractive depletion potential [46]

$$v_{\text{dep}}(r) = -\Pi_{\text{dep}}V_{\text{ex}}(r), \quad (8)$$

where  $\Pi_{\text{dep}}$  is the osmotic pressure exerted by the depletants and  $V_{\text{ex}}(r)$  is the volume from which the depletants are excluded. In general, depletion interactions depend on the size, shape, and concentration of depletants. To explore the influence of free ligands on the phase behavior of NC dispersions, we adopt a simple model that treats free ligand as a dilute gas of spherical particles of radius  $L$ , number density  $\rho_{\text{FL}}$ , and osmotic pressure  $\Pi_{\text{dep}} = \rho_{\text{FL}}k_B T$ . The excluded volume is defined by the common volume of the exclusion regions surrounding two NCs [46, 51]:

$$V_{\text{ex}}(r) = \frac{4\pi}{3}x^3 \left(1 - \frac{3r}{4x} + \frac{r^3}{16x^3}\right) \quad (9)$$

for  $1 < r < 2x$ , where  $x = 0.5 + d + L$ . In our study, we assumed a depletant radius of  $L = d/2$ . We checked, however, that the phase behavior is qualitatively the same for depletants half this size.

Assuming that free ligand is expelled from the spherical shell of adsorbed ligand, the bounds for  $v_{\text{dep}}$  are  $1 < r < 1 + 2(d + L)$ , rather than the usual hard-sphere bounds  $1 < r < 1 + 2L$  [52, 53]. Because the ligands are weakly attached to the NC surface, one might argue that the bounds should instead be  $1 + 2d < r < 1 + 2(d + L)$ . However, our choice presumes the adsorbed ligands to be relatively flexible. Also, if the bounds were taken as  $1 + 2d < r < 1 + 2(d + L)$ , then the depletion interactions would be inconsistent with  $v_{\text{el}}$  and free ligands would not contribute to self-assembly. As two NCs approach contact, it is possible that the ligands detach from the AgNC surface to maximize the interaction between ligand and solvent. This would reduce the shortest range of depletion interactions to NC core contact instead of  $1 + 2d$ , because the now-free ligands would occupy space in the spherical shell once occupied by bound ligands. Future work will focus on resolving these issues by modeling the ligands more explicitly.

For system parameters used here (Table I, Supplemental Material) [25], the effective pair potential never exhibits an attractive well deep enough for AgNC self-assembly without invoking depletion interactions. While it is possible to obtain a potential well for gold NCs coated with dodecanethiol in toluene [44], the Hildebrand solubility parameter of oley-

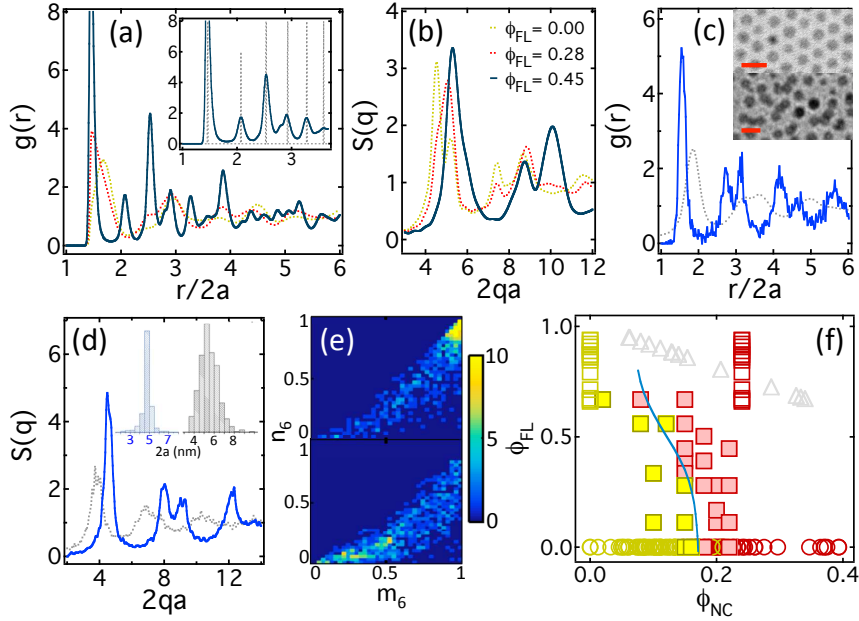


FIG. 5. (color online) (a)  $g(r)$  and (b)  $S(q)$  from simulations ( $\phi_{\text{NC}} = 0.15$ ). The inset to (a) shows a comparison with the behavior expected for a perfect 3D *fcc* crystal. The legend for free-ligand concentration ( $\phi_{\text{FL}}$ ) is shown in (b). (c) Examples of  $g(r)$  based on two different sets of TEM images, where the insets show the corresponding morphologies (10 nm scale) and (d) the corresponding  $S(q)$ , where the inset compares the two size distributions. (e) Experimental distributions in the  $(m_6, n_6)$  plane for the same images. (f) Experimental (open) and computational (closed) phase diagram delineating ordered superlattice (red/dark) and disordered ‘fluid’ (yellow/light). Open triangles represent the optically determined  $(\phi_1, \phi_2)$  data points used to deduce the open yellow/light and red/dark squares, as detailed in the text. The curve is a qualitative representation of the phase boundary based on the simulations.

lamine is considerably higher than that of dodecanethiol, implying good solvent conditions ( $\chi < 0.5$ ). Although the pair potential can be tuned somewhat by varying temperature, it would need to decrease below the freezing point of toluene to reach the poor-solvent regime ( $\chi > 0.5$ ). Figure 4 shows the effect of the depletion interactions on the effective pair potential used for the simulations [44, 47, 54–56].

To model superlattice stability, we applied Monte Carlo simulations using empirical input parameters for  $v_{\text{eff}}$  [54, 55]. We developed our code within the Open Source Physics Library [57, 58] and validated it with molecular dynamics simulations in LAMMPS [59]. We use  $g(r)$  and  $S(q)$  to distinguish order (superlattice) from disorder (gas, fluid, or aggregated

clusters). The computed  $g(r)$  at varied  $\phi_{\text{NC}}$  and  $\phi_{\text{FL}}$  (*e.g.*, Fig. 5a) and the corresponding structure factor,  $S(q)$  (Fig. 5b), are used to delineate order and disorder. To confirm superlattice, we require two criteria: (1)  $g(r)$  must exhibit peak positions consistent with an *fcc* crystal (Fig. 5a, inset), and (2)  $S(q)$  must obey the 3D Hansen-Verlet freezing criterion (HVFC), according to which the height of the main peak exceeds 2.85 for an ordered suspension. Both criteria need to be met for a system to be classified as ordered. By performing simulations over a range of initial  $\phi_{\text{NC}}$  and  $\phi_{\text{FL}}$ , we map out an equilibrium ‘phase diagram’.

#### D. Comparison of simulations & experiments

To compare simulations with experiments, we assume a core diameter of  $2a = 6$  nm and ligand of contour length  $d = 2.8$  nm (Table I, Supplemental Material). Because there is no solvent in the dried samples, experimental values of  $\phi_{\text{FL}}$  represent an upper bound. Computational details can be found in the supplementary documentation [25]. Experimentally, superlattice is evident as a splitting of the second order peak in the computed in-plane representation of  $g(r)$  (Fig. 5c) and  $S(q)$  (Fig. 5d) [60]. It can also be inferred from a locus of points (particles) near  $n_6 = m_6 = 1$  in the  $(m_6, n_6)$  plane (Fig. 5e). TEM images that showed obvious superlattice always met all of these criteria. Although the primary driver of ordering is AgNC concentration, Figs. 5c-e also highlight the critical role of size uniformity [6, 61]. The majority of the suspensions were monodisperse, but some, such as the ‘disordered’ data represented in Fig. 5c-e, were sufficiently polydisperse as to not exhibit superlattice (inset, Fig. 5d).

Figure 5f compares experiment and simulation in the form of a phase diagram in the  $\phi_{\text{NC}}\text{-}\phi_{\text{FL}}$  plane. Note that the axes are unconventional, being better suited to the experiments and simulations. We first focus on the  $\phi_{\text{FL}} = 0$ , which demonstrates the onset of order with increasing AgNC volume fraction for sufficiently monodisperse suspensions. Both simulation (closed squares, Fig. 5f) and TEM data (open circles, Fig. 5f) suggest a critical value of  $\phi_{\text{NC}}$  close to 0.17. Because the interaction potential in the absence of depletion is purely repulsive, we can rationalize this value through a solid AgNC core with a ligand layer that provides additional excluded volume. For example, including a shell of thickness  $d/2$  in our model increases the effective volume fraction from 0.17 to 0.53. In the same fashion, focusing on TEM images where superlattice was observed at the lowest core volume fraction (*e.g.*, Fig. S2b in the Supplemental Material, for suspensions with smaller mean

sizes), including a ligand shell with half the mean surface to surface separation increases the effective volume fraction to 0.61. A fluid of hard spheres freezes at a volume fraction of about 0.5 [46]. Our simulations and experiments are in reasonable agreement with this value if we account for the increase of the effective volume fraction due to the ligand shell.

Turning our attention to the presence of unbound ligand ( $\phi_{\text{FL}} > 0$ ), the other striking aspect of the computational phase diagram is the effect of depletion. The simulations clearly show that free ligand induces superlattice formation at lower  $\phi_{\text{NC}}$  than for  $\phi_{\text{FL}} = 0$ , which we associate with the emergence of an attractive effective pair potential. In the simulations, an equilibrium *fcc* crystal forms regardless of whether the NCs are initialized on a perfect lattice or in a disordered structure. For example, when we compare a system initialized in a perfect *fcc* lattice at  $\phi_{\text{NC}}=0.15$  with one in which each NC is randomly displaced by roughly 0.25 of the nearest-neighbor distance, we find that both systems first ‘melt’ and then recrystallize into an *fcc* lattice with a final volume fraction of about 0.24 ( $\phi_{\text{FL}}=0.446$ ). Our experiments are in qualitative agreement with the simulations; unbound ligand promotes order as evidenced by the presence of superlattice at global NC volumes fractions well below that anticipated for freezing (Fig. 2e). The experimental data points for  $\phi_{\text{FL}} > 0$  (open squares, Fig. 5f) were generated from optically measured  $(\phi_1, \phi_2)$  pairs (gray triangles, Fig. 5f, with  $\phi_1$  as the horizontal axis and  $\phi_2$  vertical) by taking  $\phi_{\text{F}} = 0$  (equivalent to assuming  $\phi_{\text{FL}} = \phi_2$ ) and  $\phi_{\text{NC}} = 0.25$  (the average value for  $\phi_{\text{FL}} = 0$  based on TEM). The lever rule then gives the vertical sets of open red and yellow squares in Fig. 5f.

Although our model incorporates effective interactions between adsorbed ligand shells and depletion interactions induced by free ligands, it is based on the assumption of pairwise additivity. We note, however, that the influence of nonadditivity is expected to be most profound in systems that are heterogeneous at the nanoscale, particularly with respect to charge [9]. In our system, we anticipate full ligand coverage and efficient charge screening from the metallic nanocrystal core. Thus, we attribute the success of our model to effective interactions that are pairwise additive and isotropic.

## E. Solvent effects

We also used spot-resolved optical absorption spectroscopy to probe the plasmonic response of the AgNC films. For example, the sample in Fig. 6a was cast from hexane and has a spectrum similar to the original solution; a narrow plasmon in the vicinity of 420

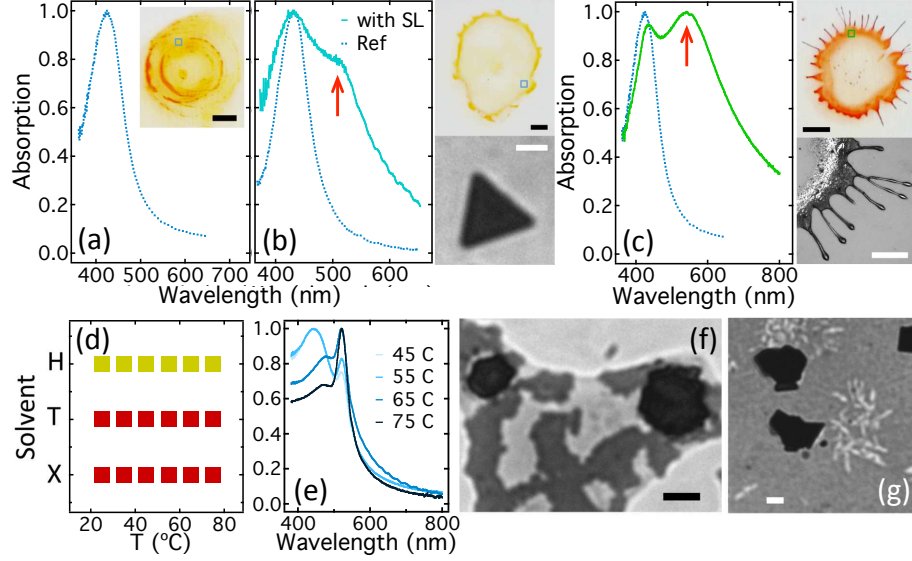


FIG. 6. (color online) (a) Absorption spectrum of AgNCs cast from hexane (ambient, inset, 1 mm scale). (b) Absorption spectra for AgNCs cast from toluene (ambient) for morphologies with (solid) and without (dashed) superlattice (SL). The upper right image corresponds to the dashed curve (1 mm scale) and the image on the lower right is an optical micrograph of a SL domain suspended in ligand (5  $\mu\text{m}$  scale). (c) Absorption spectra of dried AgNCs cast from xylene (ambient), where the dashed curve is from panel (a) (1 mm scale upper, 500  $\mu\text{m}$  scale lower). Spectra were collected at the spot indicated by the square and red arrows indicate the collective plasmon. (d) Diagram showing solvent/temperature pairs where superlattice (red/dark) was observed for hexane (H), toluene (T) and xylene (X). (e) Superlattice plasmon for a xylene suspension dried under solvent vapor at varied temperature. (f) Three-phase coexistence in a xylene/AgNC/ligand suspension dried at 25  $^{\circ}\text{C}$  (5  $\mu\text{m}$  scale) and (g) in a toluene/AgNC/ligand suspension dried at 25  $^{\circ}\text{C}$  (5  $\mu\text{m}$  scale).

nm. This tells us that the morphology at that region of the film (small square, inset Fig. 6a) is a dilute collection of weakly interacting AgNCs (a ‘gas’ or ‘fluid’). In contrast, Fig. 6b shows data collected from two films cast from toluene under different conditions; in ambient (upper right image) and slowly dried in the presence of abundant excess ligand to yield microscopic superlattice domains in a ligand-rich phase (lower right image). The former has a spectrum analogous to Fig. 6a (Fig. 6b, dashed curve), while the latter has a second peak at 510 nm (Fig. 6b, solid curve) indicative of the collective plasmonic response [17, 19–23]. Compared to the single particle plasmon, a disordered AgNC aggregate has a

broad red-shifted peak [25], while a homogeneous superlattice is characterized by a narrow modestly redshifted peak [29, 42]. We can thus use such spectra as a measure of local phase behavior [43], although care must be taken to characterize multiple regions of each sample. For example, while the sample and spectrum in Fig. 6c suggest disordered AgNC aggregates, different regions of the same film have a response more analogous to Fig. 6b, consistent with a coexistence of ordered and disordered phases.

Using the superlattice plasmon peak as a metric, we did a coarse study of phase ordering in the parameter space of solvent, solvent vapor and temperature, where experimental details can be found in the Supplemental Material [25]. Figure 6d summarizes the presence of superlattice for the solvents and temperatures considered, where red/dark markers denote the presence of superlattice, either with or without unbound ligand, when we include solvent vapor annealing. Figure 6e shows an example of superlattice emerging in droplets dried from xylene at higher temperature using solvent vapor to extend drying time. Interestingly, hexane is the only solvent for which we did not observe superlattice. Although we did observe dense nanocrystal-rich domains for samples cast from hexane with excess ligand, these domains did not have the characteristic shape or spectral signal of superlattice. Rather, we observed fluid-gas coexistence; nanocrystal-rich domains, often at the droplet surface, suspended in a ligand-rich continuous phase. The dielectric constant ranges from 2 (hexane) to 2.4 (toluene, m-xylene) and using Hildebrand solubility parameters specific to toluene and hexane yield just subtle differences in interaction potential in our model (Fig. S7, Supplemental Material) [25]. Although solvent vapor annealing can extend drying times by an order of magnitude, the longest drying times for hexane were still roughly comparable to the shortest for toluene, and we thus attribute the lack of superlattice for hexane to rapid drying times.

Not surprisingly, some of the samples showed obvious three-phase coexistence. For example, in Fig. 6f we observe superlattice domains (black) coexisting with two ligand-rich disordered phases of varied AgNC density (‘gas’ and ‘fluid’, light and dark gray, respectively), while in Fig. 6g we observe a similar coexistence in which one of the ligand-rich phases is sufficiently nanocrystal-free to crystallize (white). Neglecting pressure and any phase change on the solvent, the theoretical phase diagram of a ternary system can have at most three coexisting phases: ‘gas’ or ‘vapor’ (AgNC-poor), ‘liquid’ (AgNC-richer), and ordered solid (AgNC-richest). Indeed, three-phase coexistence is fully anticipated for



polymer-colloid mixtures [62], although our simulation method can only distinguish between fluid and solid. Kinetic effects can also influence the morphology [63, 64], however, and we have thus refrained from an analysis of three-phase data.

#### IV. CONCLUSIONS

We have quantified superlattice formation in dried suspensions of colloidal AgNCs, focusing on the role of both bound and unbound ligand. We applied Monte Carlo simulations to a coarse-grained model with an effective interaction potential that specifically accounts for ligand effects, including depletion, and the effective Hamaker constant of the nanocrystal/ligand combination. In the absence of free ligand, we find a transition to a superlattice at a AgNC core volume fraction of 0.17. Because the effective potential is purely repulsive in this limit, we attribute this behavior to additional excluded volume associated with the AgNC ligand shell, which gives an effective volume fraction close to that anticipated for hard-sphere freezing [46].

Both simulation and experiment identify free ligand as an effective depletant for promoting superlattice formation in ternary AgNC/ligand/solvent mixtures. In the presence of such depletants, the effective potential becomes attractive and phase ordering occurs at lower nanocrystal core volume fractions in the superlattice phase. The experiments in this limit show multiphase coexistence typical of polymer-colloid mixtures, with solvent vapor annealing providing a potential route to controlling phase ordering through extended drying times and fuller equilibration.

#### V. ACKNOWLEDGEMENTS

The authors acknowledge the support of the National Science Foundation (NSF) through CBET-1603445.

- 
- [1] C. B. Murray, C. R. Kagan, M. G. Bawendi, *Science* **270**, 1335 (1995).
  - [2] D. Vanmaekelbergh, *Nano Today* **6**, 419 (2011).

- [3] M. A. Boles, M. Engel, D. V. Talapin, *Chem. Rev.* **116**, 11220 (2016).
- [4] X. M. Lin, H. M. Jaeger, C. M. Sorensen, K. J. Klabunde, *J. Phys. Chem. B* **105**, 3353 (2001).
- [5] J. Park, H. Zheng, W. C. Lee, P. L. Geissler, E. Rabani, A. P. Alivisatos, *ACS Nano* **6**, 2078 (2012).
- [6] C. B. Murray, C. R. Kagan, M. G. Bawendi, *Annu. Rev. Mater. Sci.* **30**, 545 (2000).
- [7] M. I. Bodnarchuk, M. V. Kovalenko, W. Heiss, D. V. Talapin, *J. Am. Chem. Soc.* **132**, 11967 (2010).
- [8] W. H. Evers, B. De Nijs, L. Filion, S. Castillo, M. Dijkstra, D. Vanmaekelbergh, *Nano Lett.* **10**, 4235 (2010).
- [9] C. A. Silvera Batista, R. G. Larson, N. A. Kotov, *Science* **350**, 1242477 (2015).
- [10] C. D. Ma, C. Wang, C. Acevedo-Vélez, S. H. Gellman, N. L. Abbott, *Nature* **517**, 347 (2015).
- [11] B. W. Kwaadgras, M. W. J. Verdult, M. Dijkstra, R. van Roij, *J. Chem. Phys.* **138**, 104308 (2013).
- [12] K. Barros and E. Luijten, *Phys. Rev. Lett.* **113**, 017801 (2014).
- [13] B. W. Goodfellow, Y. Yu, C. A. Bosoy, D.-M. Smilgies, B. A. Korgel, *J. Phys. Chem. Lett.* **6**, 2406 (2015).
- [14] J. B. Miller, A. R. Van Sickle, R. J. Anthony, D. M. Kroll, U. R. Kortshagen, E. K. Hobbie, *ACS Nano* **6**, 7389 (2012).
- [15] J. B. Miller, A. C. P. Usselman, R. J. Anthony, U. R. Kortshagen, A. J. Wagner, A. R. Denton, E. K. Hobbie, *Soft Matter* **10**, 1665 (2014).
- [16] Y. Yu, C. A. Bosoy, C. M. Hessel, D.-M. Smilgies, B. A. Korgel, *Chem. Phys. Chem.* **14**, 84 (2013).
- [17] H. Wang, D. W. Brandl, P. Nordlander, N. J. Halas, *Acc. Chem. Res.* **40**, 53 (2007).
- [18] M. Hentschel, M. Saliba, R. Vogelgesang, H. Giessen, A. Paul Alivisatos, N. Liu, *Nano Lett.* **10**, 2721 (2010).
- [19] J. A. Fan, C. Wu, K. Bao, J. Bao, R. Bardhan, N. J. Halas, V. Manoharan, P. Nordlander, G. Shvets, F. Capasso, *Science* **328**, 1139 (2010).
- [20] G. Sun and J. B. Khurgin, *Appl. Phys. Lett.* **97**, 263110 (2010).
- [21] J. C. Fraire, L. A. Pérez, Eduardo A. Coronado, *ACS Nano* **6**, 3441 (2012).
- [22] B. Yan, S. V. Boriskina, Björn M. Reinhard, *J. Phys. Chem. C* **115**, 24437 (2011).
- [23] W. Ahn, S. V. Boriskina, Y. Hong, Björn M. Reinhard, *Nano Letters* **12**, 219 (2012).

- [24] I. Valmianski, *Two point correlation function of a finite 2D lattice* ([www.mathworks.com](http://www.mathworks.com)).
- [25] See Supplemental Material at [URL will be inserted by publisher] for AgNC size distributions, DGU details, and additional computational and experimental details.
- [26] H. Hiramatsu and F. E. A. Osterloh, *Chem. Mater.* **16**, 2509 (2004).
- [27] J. B. Miller, J. M. Harris, E. K. Hobbie, *Langmuir* **30**, 7936 (2014).
- [28] J. B. Miller and E. K. Hobbie, *J. Polym. Sci., Part B: Polym. Phys.* **51**, 1195 (2013).
- [29] J. Wei, N. Schaeffer, P.-A. Albouy, M. P. Pileni, *Chem. Mater.* **27**, 5614 (2015).
- [30] J. A. Scholl, A. L. Koh, J. A. Dionne, *Nature* **483**, 421 (2012).
- [31] J. J. Wei, N. Schaeffer, M. P. Pileni, *J. Phys. Chem. B* **118**, 14070 (2014).
- [32] C. Y. Lau, H. Duan, F. Wang, C. B. He, H. Y. Low, J. K. W. Yang, *Langmuir* **27**, 3355 (2001).
- [33] D. K. Smith, B. Goodfellow, D.-M. Smilgies, B. A. Korgel, *J. Am. Chem. Soc.* **131**, 3281 (2009).
- [34] D. Baranov, A. Fiore, M. van Huis, C. Giannini, A. Falqui, U. Lafont, H. Zandbergen, M. Zanella, R. Cingolani, L. Manna, *Nano Lett.* **10**, 743 (2010).
- [35] M. Zanella, G. Bertonni, I. R. Franchini, R. Brescia, D. Baranov, L. Manna, *Chem. Comm.* **47**, 203 (2011).
- [36] K. L. Young, M. R. Jones, J. Zhang, R. J. Macfarlane, R. Esquivel-Sirvent, R. J. Nap, J. Wu, G. C. Schatz, B. Lee, C. A. Mirkin, *Proc. Natl. Acad. Sci. U.S.A.* **109**, 2240 (2012).
- [37] J. Henzie, M. Grunwald, A. Widmer-Cooper, P. L. Geissler, P. Yang, *Nature Mat.* **11**, 131 (2012).
- [38] A. S. Karas, J. Glaser, S. C. Glotzer, *Soft Matter* **12**, 5199 (2016).
- [39] In 3D (simulations),  $S(q) = 1 + \frac{2}{N} \sum_{i < j=1}^N \left\langle \frac{\sin(qr_{ij})}{qr_{ij}} \right\rangle$ , while in 2D (TEM),  $S(q) = 1 + \frac{2}{N} \sum_{i < j=1}^N \langle J_0(qr_{ij}) \rangle$ , where  $J_0$  is the zeroth-order Bessel function of the first kind.
- [40] A. E. Larsen and D. J. Grier, *Phys. Rev. Lett.* **76**, 3862 (1996).
- [41] P. Dillmann, G. Maret, P. Keim, *J. Phys.: Condens. Matter* **24**, 464118 (2012).
- [42] S. Zou, N. Janel, G. C. Schatz, *J. Chem. Phys.* **120**, 10871 (2004).
- [43] We make no attempt to correlate peak height with the volume fraction of the associated phase but simply use it to identify its presence.
- [44] S. J. Khan, F. Pierce, C. M. Sorenson, A. Chakrabarti, *Langmuir* **25**, 13861 (2009).
- [45] N. Goubet, J. Richardi, P. A. Albouy, M. P. Pileni, *J. Phys. Chem. Lett.* **2**, 417 (2011).

- [46] R. A. L. Jones, *Soft Condensed Matter* (Oxford University Press, Oxford, United Kingdom, 2002).
- [47] J. N. Israelachvili, *Intermolecular and Surface Forces* (Elsevier, Waltham, 2011).
- [48] R. Evans and D. H. Napper, *Kolloid-Z. u. Z. Polymere* **251**, 329 (1973).
- [49] J. B. Smitham, R. Evans, D. H. Napper, *J. Chem. Soc., Faraday Trans.* **71**, 285 (1975).
- [50] R. Evans, J. B. Smitham, D. H. Napper, *Colloid Polym. Sci.* **255**, 161 (1977).
- [51] X. Ye, T. Narayanan, and P. Tong, *Phys. Rev. Lett.* 1996, **76**, 4640 (1996).
- [52] S. Asakura and F. Oosawa, *J. Chem. Phys.* **22**, 1255 (1954).
- [53] F. Oosawa and S. Asakura, *J. Chem. Phys.* **22**, 1255 (1954).
- [54] A. O. Pinchuk, *J. Phys. Chem. C* **116**, 20099 (2012).
- [55] A. Evelyn Di Mauro, M. Striccoli, N. Depalo, E. Fanizza, L. Cano, C. Ingrosso, A. Agostiano, M. Lucia Curri, A. Tercjak, *Soft Matter* **10**, 1676 (2014).
- [56] A. Fernández-Nieves, A. Fernández-Barbero, B. Vincent, and F. J. de las Nieves, *Langmuir* **17**, 1841 (2001).
- [57] H. Gould, J. Tobochnik, W. Christian, *An Introduction to Computer Simulation Methods: Applications to Physical Systems* (Addison-Wesley, 3<sup>rd</sup> edition, 2006).
- [58] D. Frenkel, B. Smit, *Understanding Molecular Simulation: From Algorithms to Applications* (Academic Press, 2<sup>nd</sup> edition, 2002).
- [59] S. Plimpton, *J. Comp. Phys.* **117**, 1 (1995).
- [60] The HVFC becomes modified in 2D such the the peak value in  $S(q)$  for crystallization is between 4.4 and 5.5. See, for example, Z. Wang, A. M. Alsayed, A. G. Yodh, Y. Han, *J. Chem. Phys.* **132**, 154501 (2010).
- [61] S. Auer and D. Frenkel, *Nature* **413**, 711 (2001).
- [62] H. N. W. Lekkerkerker, W. C.-K. Poon, P. N. Pusey, A. Stroobants, P. B. Warren, *Europhys. Lett.* **20**, 559 (1992).
- [63] A. J. Wagner and J. M. Yeomans, *Phys. Rev. Lett.* **80**, 1429 (1998).
- [64] G. Ge and L. Brus, *J. Phys. Chem. B* **104**, 9573 (2000).